

Research Article

Current PI^λ Control of the Single-Phase Grid Inverter

Xueqin Yang,¹ Xingyu Liu,¹ Jichao Li,² and Binbin Zhang² 

¹*School of Communications and Information Engineering & School of Artificial Intelligence, Xi'an University of Posts & Telecommunications, Xi'an 710021, Shaanxi Province, China*

²*School of Electronic Information Engineering, Xi'an Technological University, Xi'an 710021, Shaanxi Province, China*

Correspondence should be addressed to Binbin Zhang; zbb521zbb@126.com

Received 2 June 2021; Revised 3 October 2021; Accepted 19 October 2021; Published 8 November 2021

Academic Editor: Omar Naifar

Copyright © 2021 Xueqin Yang et al. This is an open access article distributed under the Creative Commons Attribution License, which permits unrestricted use, distribution, and reproduction in any medium, provided the original work is properly cited.

In a grid-connected power generation system, the grid-connected current of the inverter is sensitive to nonlinear factors such as periodic disturbance of grid voltage, which results in grid-connected current waveform distortion. By establishing a single-phase photovoltaic grid-connected inverter control system model, designing an inverse current fractional-order PI (PI^λ or FO-PI) controller and the dynamic and steady-state performance, antidisturbance and grid connection inversion characteristics of the system are simulated and compared under the action of the integer-order PI controller and fractional-order PI controller. The quality of the inverter grid-connected current is analyzed by using the fast Fourier transform (FFT). The simulation results show that the fractional-order control system can reduce the total harmonic distortion (THD) of the grid-connected current and dynamic performance and antidisturbance ability of the improving system while satisfying the steady-state performance indexes.

1. Introduction

Solar grid-connected photovoltaic (PV) system has great strategic significance to alleviate the current energy crisis and environmental pollution. Inverter as the core of the grid-connected PV system, the output of the grid-connected current directly affects the power quality of the power grid. Therefore, it is of great practical significance to study an effective grid-connected current control strategy so that the photovoltaic system can realize the grid-connected operation while the total harmonic distortion (THD) of the grid-connected current is as small as possible.

The common current digital control strategies of the grid-connected current are PI control, voltage and current double-closed loop control, repetitive control, no beat control, and so on. The PI control strategy is widely used in engineering because of its simple control method, easy implementation, and good dynamic performance. In literature [1], the parameters of the PI controller are self-tuned by using the principle of fuzzy control, which effectively reduces the current tracking error and improves the dynamic response performance of the system. In this method, the parameter of the controlled object is relatively rough,

and the fuzzy inference is more dependent on the rich engineering experience. Literature [2] proposes a current-tracking control strategy combining repetitive control and PI control, which can effectively improve the grid-connected current waveform and ensure that the inverter output current and grid voltage are with the same frequency and phase, but their dynamic response is poor. In literature [3], different duty ratio control functions are generated by the controller to control the output current of the grid-connected inverter. The output power quality of the inverter is relatively stable, but the response speed of the system is slow, and the application scope is small. In literature [4], combined with repetitive control and H_∞ control, an inverter current controller is designed to improve the tracking performance of the system and reduce the total harmonic distortion (THD). However, the method needs to solve the Riccati equation, and the operation is more complex, so the method cannot be widely used. In literature [5], a composite control strategy based on internal model control and repetitive control is proposed by using the internal model control to simplify the parameters of the controller in order to achieve the purpose of improving the dynamic performance of the system and the repetitive control to suppress

the disturbance of the power grid in order to achieve the purpose of improving the steady-state performance of the system. This method requires that the filter has low-pass characteristics, but in practice, any high-frequency signals cannot achieve the desired results.

In view of the above problems, this paper based on the analysis of the current waveform distortion causes of the single-phase PV grid-connected inverter, combined with the PI^λ controller flexible control structure; when it acts on the controlled object, the system has better dynamic, steady-state performance, and robustness [6, 7]; the PI^λ controller is applied to the single-phase PV grid-connected power generation system. Starting from the control structure of the grid-connected inverter and taking the inverter output current as the control object, the inverter control model is established, PI^λ controller is designed, and the MATLAB/Simulink simulation model is set up; the performance of the control system is simulated and compared with the PI^λ controller and the integer-order PI controller, and the effectiveness of the control strategy is verified.

2. Single-Phase PV Grid-Connected Inverter Control Strategy

The output of the grid-connected inverter adopts the current control mode. Actually, the grid-connected system and the grid are AC sources and voltage sources in parallel. The output voltage of the inverter is automatically clamped to the grid voltage. Therefore, it is only needed to control the output current of the inverter that tracks the grid voltage to achieve the purpose of the grid-connected operation. This paper adopts the control strategy of current instantaneous value feedback and triangular wave comparison, and the controller uses the fractional-order proportional-integral (FO- PI^λ) control method.

2.1. Grid-Connected Inverter Control Structure. In the single-phase PV grid-connected inverter control structure as shown in Figure 1, the main circuit uses the two-level topology: boost type DC/DC step-up chopper circuit is formed by pre-energy storage inductor L1, IGBT switch tube VT1, and rectifier diode D0, mainly to achieve the PV terminal voltage to the required voltage of the grid. The latter stage is composed of four IGBT switches to form a DC/AC full-bridge inverter circuit, which can realize the grid-connected current and grid voltage with the same frequency and phase control and DC bus voltage stability. C_{pv} for the PV output side of the storage capacitor is used to stabilize the PV module output DC voltage and C_{dc} is the storage capacitor of the inverter DC side.

The specific control process is as follows: compared with the difference between grid-connected current reference value i_{ref} and the actual value of the grid-connected current i_s , adjusted by the PI^λ controller and compared with the triangular modulation wave, the SPWM control signal is generated to drive the switching tube of the inverter, and inverter output is filtered through the inductor L and fed into the same frequency and phase with the grid voltage sine wave current i_s .

2.2. The System Control Model. During the grid operation, switch frequency (10 kHz) is much higher than the grid voltage rated frequency (50 Hz); therefore, it can ignore the switch delay and switch off action effects on the system, and the full-bridge inverter is approximated as a link gain of K . Design grid-connected current control block diagram [8, 9], as shown in Figure 2.

In Figure 2, $G_c(s)$ is the transfer function of the controller, L is the filter inductor, and R is the equivalent resistance of the filter inductor. Assuming the power switch as an idealized switch, the transfer function of the full-bridge inverter in the SPWM control mode can be approximated as a small inertia link [10], that is, $K_{inv}/(sT_{inv} + 1)$, where K_{inv} is the gain of the inverter and T_{inv} is the switching time period. From the analysis of literature [11], it can be seen that the influence of grid voltage disturbance on the system can be neglected when the controller parameters are reasonable, and the mathematical model of the control object can be obtained as

$$G_s(s) = \frac{K_{inv}}{sT_{inv} + 1} \cdot \frac{1}{sL + R} = \frac{K_{inv}}{sT_{inv} + 1} \frac{(1/R)}{s(L/R) + 1}. \quad (1)$$

3. PI^λ Controller Design

3.1. $PI^\lambda D^\mu$ Controller. $PI^\lambda D^\mu$ controller is proposed by Professor I. Podlubny [12], and the transfer function is

$$G_c(s) = K_p + \frac{K_i}{s^\lambda} + K_d s^\mu. \quad (2)$$

$PI^\lambda D^\mu$ controller includes an integral order λ and a differential order μ , where λ and μ can be arbitrary real numbers. In the design of a fractional-order control system, the controller parameters K_p , K_i , K_d , λ , and μ must be optimized to meet the requirements according to the performance index of the system.

From formula (2), when λ and μ take different combinations, respectively, $(\lambda, \mu) = \{(0, 0), (0, 1), (1, 0), (1, 1)\}$, it can be obtained as a conventional proportional (P) controller, a PD controller, a PI controller, and a PID controller. The value plane of λ and μ is shown in Figure 3.

As can be seen from the figure, the conventional PID controller is a special case of the $PI^\lambda D^\mu$ controller. Since λ and μ can vary continuously, the $PI^\lambda D^\mu$ controller is more flexible than the integer-order PID controller [13, 14]. By selecting the values of λ and μ reasonably, the dynamic performance of the fractional-order control system can be better adjusted.

3.2. PI^λ Controller Design. The $PI^\lambda D^\mu$ controller transfer function is expressed by formula (2), which makes $\mu = 0$, and then the transfer function of the PI^λ controller can be obtained:

$$G_c(s) = K_p + \frac{K_i}{s^\lambda}. \quad (3)$$

In order to facilitate the analysis, formula (3) can be rewritten as

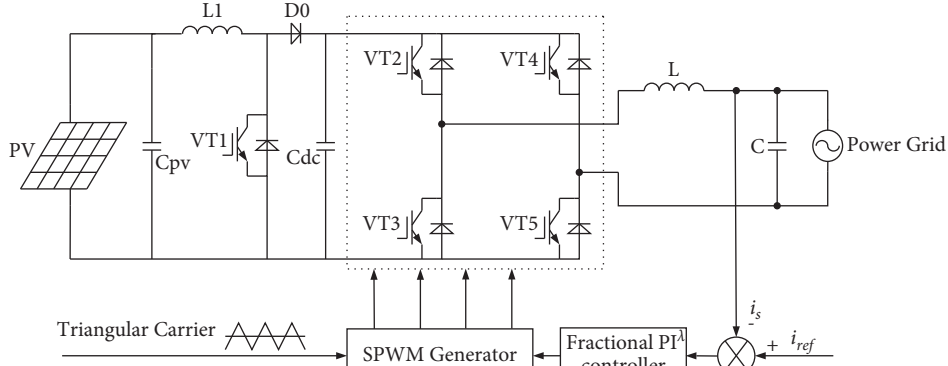


FIGURE 1: Main circuit inverter control structure.

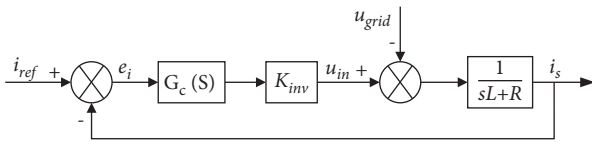


FIGURE 2: Block diagram of grid-connected current control.

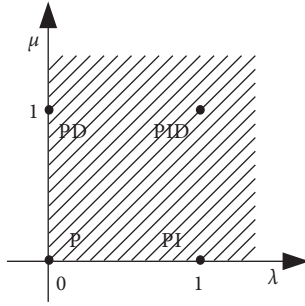


FIGURE 3: P-I-D order value plane.

$$G_c(s) = K_p \left(1 + \frac{K'_i}{s^\lambda} \right) \quad (K_i = K_p K'_i). \quad (4)$$

For the specific control object $G_s(s)$, the parameters of the PI^λ controller are optimized by using the frequency characteristic of the control system and the given cut-off frequency ω_c and the phase margin ϕ_m . The open-loop transfer function $G_k(s)$ can satisfy the following performance index by designing the PI^λ controller $G_c(s)$ [15]:

(1) Phase margin:

$$\begin{aligned} \text{Arg}[G_k(j\omega_c)] &= \text{Arg}[G_c(j\omega_c)G_s(j\omega_c)] \\ &= -\pi + \phi_m. \end{aligned} \quad (5)$$

(2) Gain robustness:

$$\left(\frac{d(\text{Arg}(G_c(j\omega)G_s(j\omega)))}{d\omega} \right)_{\omega=\omega_c} = 0. \quad (6)$$

(3) Amplitude criterion:

$$|G_k(j\omega_c)| = |G_c(j\omega_c)G_s(j\omega_c)| = 1. \quad (7)$$

The frequency response of the PI^λ controller is obtained by formula (4) combined with the Euler's formula:

$$G_c(j\omega) = K_p \left[\left(1 + K'_i \omega^{-\lambda} \cos \frac{\lambda\pi}{2} \right) - j K'_i \omega^{-\lambda} \sin \frac{\lambda\pi}{2} \right]. \quad (8)$$

Its phase and amplitude are

$$\text{Arg}[G_c(j\omega)] = -\arctan \left(\frac{K'_i \omega^{-\lambda} \sin(\lambda\pi/2)}{1 + K'_i \omega^{-\lambda} \cos(\lambda\pi/2)} \right), \quad (9)$$

$$|G_c(j\omega)| = K_p \sqrt{\left(K'_i \omega^{-\lambda} \sin \frac{\lambda\pi}{2} \right)^2 + \left(1 + K'_i \omega^{-\lambda} \cos \frac{\lambda\pi}{2} \right)^2}. \quad (10)$$

For the controlled object $G_s(s)$, the inverter gains K_{inv} and $1/R$ can be transferred to the proportional gain K_p of the controller without affecting the gain of the whole inverter control link [16]. Therefore, for the sake of generality, the gain and $1/R$ in formula (1) are normalized to 1. At this point, there is

$$K'_p = \frac{1}{R} K_p K_{inv}. \quad (11)$$

The frequency response of the controlled object is

$$G_s(j\omega) = \frac{1}{j\omega T_{inv} + 1} \cdot \frac{1}{j\omega(L/R) + 1}. \quad (12)$$

Its phase and amplitude are

$$\text{Arg}[G_s(j\omega)] = -\arctan(\omega T_{inv}) - \arctan\left(\omega \frac{L}{R}\right), \quad (13)$$

$$|G_s(j\omega)| = \frac{1}{\sqrt{1 + (\omega T_{inv})^2} \cdot \sqrt{1 + (\omega(L/R))^2}}. \quad (14)$$

The open-loop transfer function is

$$G_k(s) = G_c(s) \cdot G_s(s). \quad (15)$$

From formulas (9), (13), and (15), the phase angle of the open-loop transfer function is

$$\begin{aligned}
\text{Arg}(G_k(j\omega)) &= \text{Arg}(G_c(j\omega)) + \text{Arg}(G_s(j\omega)) \\
&= -\arctan\left(\frac{K_i \omega^{-\lambda} \sin(\lambda\pi/2)}{1 + K_i \omega^{-\lambda} \cos(\lambda\pi/2)}\right) \\
&\quad - \arctan(\omega T_{\text{inv}}) - \arctan\left(\omega \frac{L}{R}\right).
\end{aligned} \tag{16}$$

From formulas (10), (14), and (15), the amplitude of the open-loop transfer function is

$$\begin{aligned}
|G_k(j\omega)| &= |G_c(j\omega)G_s(j\omega)| \\
&= \frac{K_p \sqrt{(1 + K_i \omega^{-\lambda} \cos(\lambda\pi/2))^2 + (K_i \omega^{-\lambda} \sin(\lambda\pi/2))^2}}{\sqrt{1 + (\omega T_{\text{inv}})^2} \sqrt{1 + (\omega(L/R))^2}}.
\end{aligned} \tag{17}$$

From formula (16) and the phase angle margin criterion, the relationship between K'_I and λ can be obtained as

$$K'_I = \frac{-\tan[\arctan(\omega_c T_{\text{inv}}) + \arctan(\omega_c(L/R)) + \phi_m - \pi]}{\omega_c^{-\lambda} \sin \lambda\pi/2 + \omega_c^{-\lambda} \cos \lambda\pi/2 \tan[\arctan(\omega_c T_{\text{inv}}) + \arctan(\omega_c(L/R)) + \phi_m - \pi]}. \tag{18}$$

From formula (16) and the robustness criterion, another relation between K'_I and λ can also be established:

$$K'_I = \frac{-B \pm \sqrt{B^2 - 4A^2 \omega_c^{-2\lambda}}}{2A \omega_c^{-2\lambda}}, \tag{19}$$

where

$$\begin{cases} A = \frac{T_{\text{inv}}}{1 + (\omega_c T_{\text{inv}})^2} + \frac{(L/R)}{1 + (\omega_c(L/R))^2}, \\ B = 2A \omega_c^{-\lambda} \cos \frac{\lambda\pi}{2} - \lambda \omega_c^{-\lambda-1} \sin \frac{\lambda\pi}{2}. \end{cases} \tag{20}$$

From Formula (17) and the amplitude criterion, we obtain the equation for K_p :

$$K_p = \frac{\sqrt{1 + (\omega_c(L/R))^2} \sqrt{1 + (\omega_c T_{\text{inv}})^2}}{\sqrt{(1 + K'_I \omega_c^{-\lambda} \cos(\lambda\pi/2))^2 + (K'_I \omega_c^{-\lambda} \sin(\lambda\pi/2))^2}}. \tag{21}$$

On the basis of satisfying the phase angle margin criterion, the robustness criterion, and the amplitude criterion, the relations of λ and K_p and λ and K_i are obtained. It is shown that, in the PI^λ controller, the change of λ will affect the response speed, overshoot, adjustment time, and steady-state error of the system through the proportional and integral links.

In order to obtain a relatively satisfactory transient response, the photovoltaic grid-connected control system phase angle margin is generally between $30^\circ \sim 60^\circ$; the cut-off frequency is 200 rad/s \sim 300 rad/s [17]. The given phase angle margin and the expected value of the cut-off frequency are shown in Table 1.

By using the plotting method, three parameters of the PI^λ controller are obtained: $K_p = 7.89$, $K_i = 73.25$, and $\lambda = 0.535$. According to formulas (18)–(21) and $K_i = K_p \cdot K'_I$, we can write the PI^λ controller transfer function as

$$G_c(s) = 7.89 + \frac{73.25}{s^{0.535}}. \tag{22}$$

4. PI^λ Controller Performance Analysis Diagnosis

4.1. The Oustaloup Approximation of Integral Operator s^λ . The integral operator s^λ is approximated by the Oustaloup algorithm in the transfer function expression of the FO-PI controller [17]. The algorithm can guarantee the approximation of the fractional transfer function on the basis of stability so that the transfer function is as little as possible to the zero and the pole. Assuming that the selected approximation bands are ω_b and ω_h , the algorithm is described as

$$s^\lambda \approx K \prod_{k=-N}^N \frac{s + \omega'_k}{s + \omega_k}. \tag{23}$$

In this formula,

$$\begin{cases} \omega'_k = \omega_b \left(\frac{\omega_h}{\omega_b} \right)^{(k+N+0.5(1-\lambda))/(2N+1)}, \\ K = \omega_h^\lambda, \\ \omega_k = \omega_b \left(\frac{\omega_h}{\omega_b} \right)^{(k+N+0.5(1+\lambda))/(2N+1)}. \end{cases} \tag{24}$$

Formula (24) can be considered as a recursion filter (IIR) with the order $n = 2N + 1$. When the approximation order $n = 1$, the approximation error is large. When the approximation order $n = 5$, both the amplitude-frequency characteristic and the phase-frequency characteristic can well approximate the fractional order. The higher the approximation order is, the higher the approximation accuracy will be. But when n is more than 5, the approximation accuracy and the approximation order are no longer proportional [18]. So, the third-order inner approximation is considered to use. The high-order term $1/s^\lambda$ of the FO-PI controller is approximated in the frequency band of interest ($\omega_b = 0.001$ Hz and $\omega_h = 1000$ Hz) with $n = 3$, i.e., $N = 1$. The approximate result is

TABLE 1: System parameter.

System parameters	Parameter value
Cutoff frequency desired value, ω_c	200 rad/s
Phase angle margin expected value, φ_m	60°
Switching time period, T_{inv}	$100 \mu s$
Equivalent resistance, R	0.5Ω
Filter inductance, L	6 mH

$$\frac{1}{s^\lambda} = \frac{0.024831(s + 342.8)(s + 3.428)(s + 0.03428)}{(s + 29.17)(s + 0.2917)(s + 0.002917)}. \quad (25)$$

4.2. The Dynamic and Steady-State Performance Analysis. In the integral PI controller, the integral $K_i s^{-1}$ is mainly used to improve the steady-state performance of the system. But because of the 90° lag phase angle of the integral, the overshoot and the adjustment time of the system are increased, and the dynamic performance of the system is poor. λ of $K_i s^{-\lambda}$ can be adjusted arbitrarily, and the adjustment accuracy is high. The stability and dynamic performance of the system can be taken into account under the premise of improving the steady-state characteristics of the system. Figure 4 shows the unit step response curve for different values of λ .

From Figure 4, it can be seen that, with the increment of λ , the steady-state accuracy of the system is obviously improved, the adjustment time is gradually reduced, and the overshoot quantity decreases gradually. The value of λ continues to increase, and the adjustment time becomes larger. The steady-state accuracy is reduced, and oscillation occurs. Therefore, the integral order λ mainly affects the steady-state error of the system. Selecting the proper integration order can reduce the steady-state error of the system and obtain a good dynamic performance.

Let $\lambda = 1$ and $\mu = 0$ in formula (2), then the integral-order PI controller transfer function can be expressed as

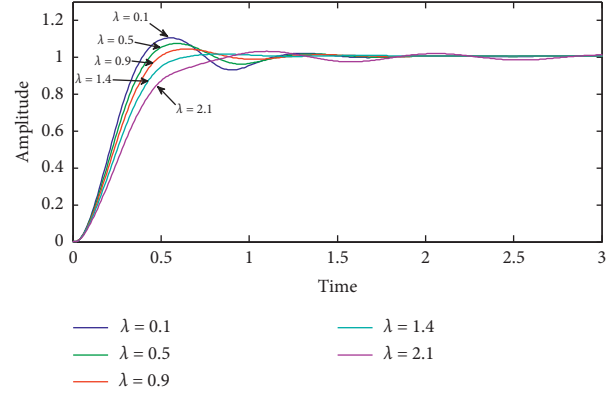
$$G_{c1}(s) = K_{p1} + \frac{K_{i1}}{s}. \quad (26)$$

The parameters of the PI controller are obtained by the method of engineering design, that is, $K_{p1} = 0.13$ and $K_{i1} = 10.79$, and the transfer function of the integer-order PI controller is

$$G_{c1}(s) = 0.13 + \frac{10.79}{s}. \quad (27)$$

In the MATLAB/Simulink environment, a step-by-step simulation model is set up. Taking the step signal as the input, the control object is controlled by the PI controller and the integer-order PI controller; the simulation results are shown in Figure 5.

The main performance indexes of the FO-PI controller and the IO-PI controller are obtained from the step response curve: rise time t_r , overshoot δ , and adjustment time t_s ($\pm 2\%$ steady-state value), as shown in Table 2. It can be seen that the dynamic follow-up performance of the system using the FO-PI controller is superior to the system using the IO-PI controller.

FIGURE 4: Comparison of step response as λ varies.

To further verify the validity of the designed FO-PI controller parameters and the superiority of the control performance, the Bode diagram of the open-loop system under FO-PI and IO-PI controller is obtained, as shown in Figure 6.

In order to control the two control effects of comparative analysis more intuitively, the performance index values in the chart are tabulated, as shown in Table 3.

As the results shown in Figure 6 and Table 3, the following conclusions can be drawn:

- (1) When the system is stable, the FO-PI control system is closer to the expected phase margin and cutoff frequency than the IO-PI control system that the phase margin criterion is met.
- (2) The robustness criterion (at the cutoff frequency): the first derivative of the phase is 0, the derivative at point A and point B on the curve of the FO-PI control system in Figure 6 is 0, which satisfies the criterion of robustness.
- (3) When the FO-PI control system is in the cutoff frequency, the amplitude variation is 0, which meets the criterion of amplitude.

4.3. System Antidisturbance Analysis. Considering the influence of grid voltage, the transfer function of the output current of the grid-connected inverter is produced in Figure 2.

$$i_s = \frac{KG(s)}{Ls + R + KG(s)} i_{ref} - \frac{1}{Ls + R + KG(s)} u_{grid}. \quad (28)$$

Substituting the fundamental frequency ω_0 into equation (26), the amplitude of IO-PI controller is obtained: $A(\omega_0)_1 = \sqrt{K_{p1}^2 + (K_{i1}/\omega_0)^2}$, which is a finite value. Let the first term in equation (28) be $\varepsilon \cdot i_{ref}$, where $\varepsilon = (KG(s)/(Ls + R + KG(s))) = 1/(1 + (Ls + R_L/KG(s)))$; it can be seen that $0 < |\varepsilon| < 1$, the output current is less than the reference current, and the system has steady-state errors. Similarly, the second term is also a limited value, that the inverter output current is affected by the grid voltage; the system's anti-interference ability is poor.

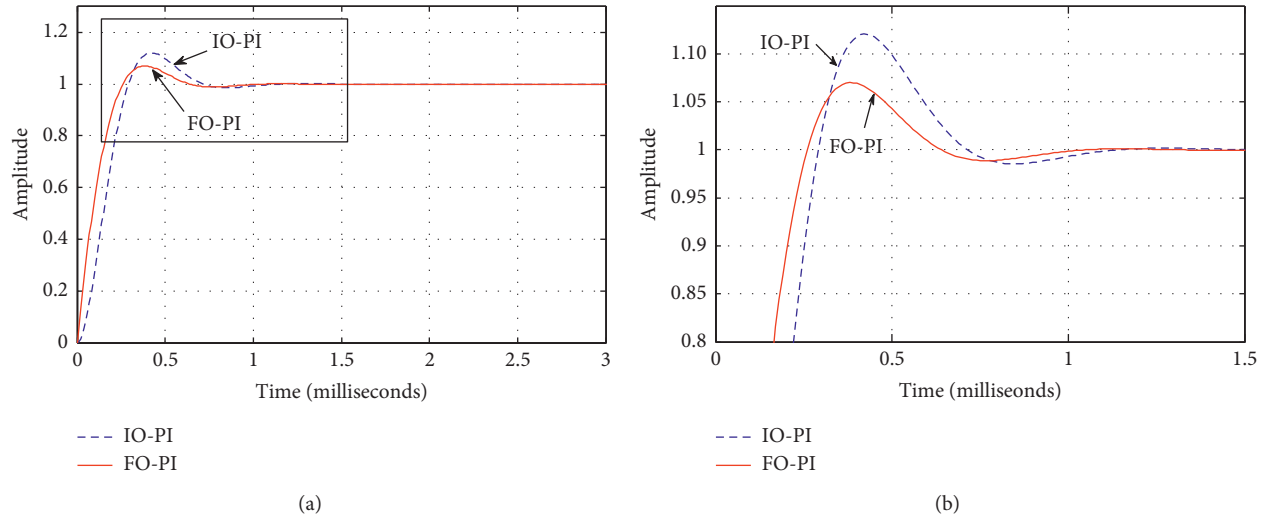


FIGURE 5: System step response curve. (a) Step response curve (b) Local magnification.

TABLE 2: Dynamic performance index.

Controller	tr (ms)	δ (%)	ts (ms)
IO-PI	0.29	12	1.08
FO-PI	0.26	6.9	1.02

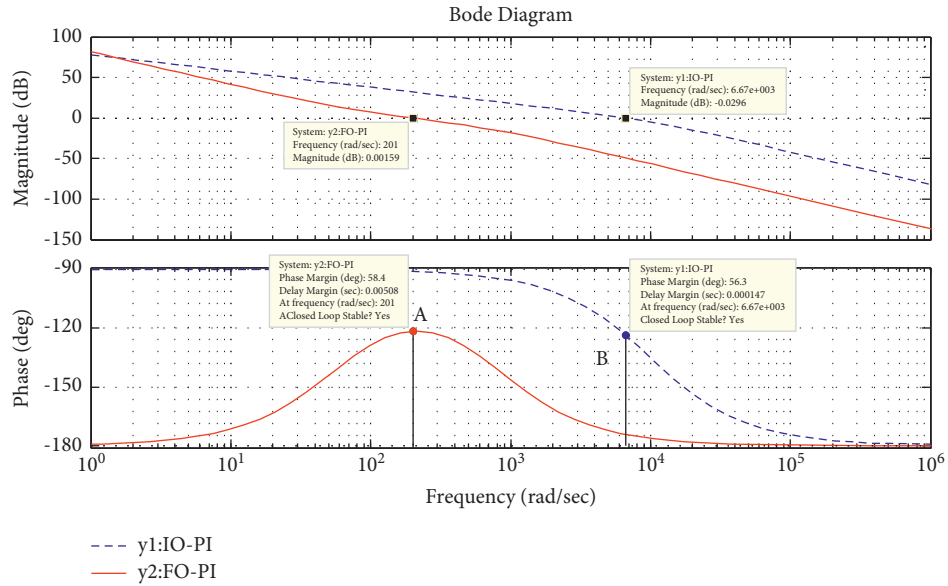


FIGURE 6: Open-loop transfer function: Bode diagram.

TABLE 3: Open-loop system performance.

Performance index	When the system is stable		
	Expected value	FO-PI	IO-PI
Phase margin (Xo)	60	58.4	56.3
Amplitude variation (dB)	0	0.0061	0.0296
Cut-off frequency (rad/s)	200	201	6.67×10^3

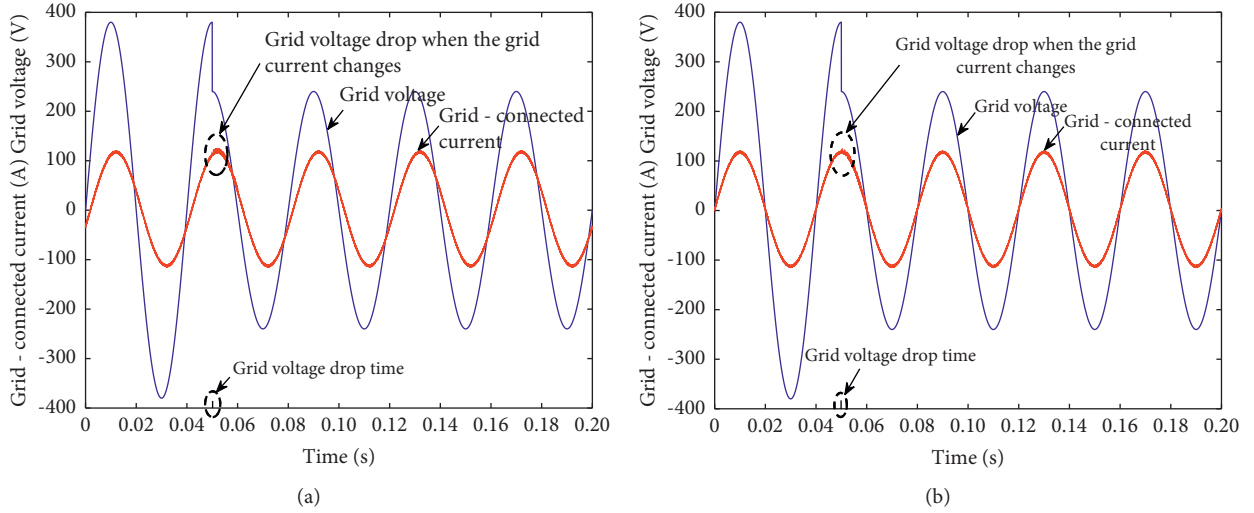


FIGURE 7: output current waveform of the inverter in the grid voltage change. Simulation waveforms under (a) IO-PI control and (b) FO-PI control.

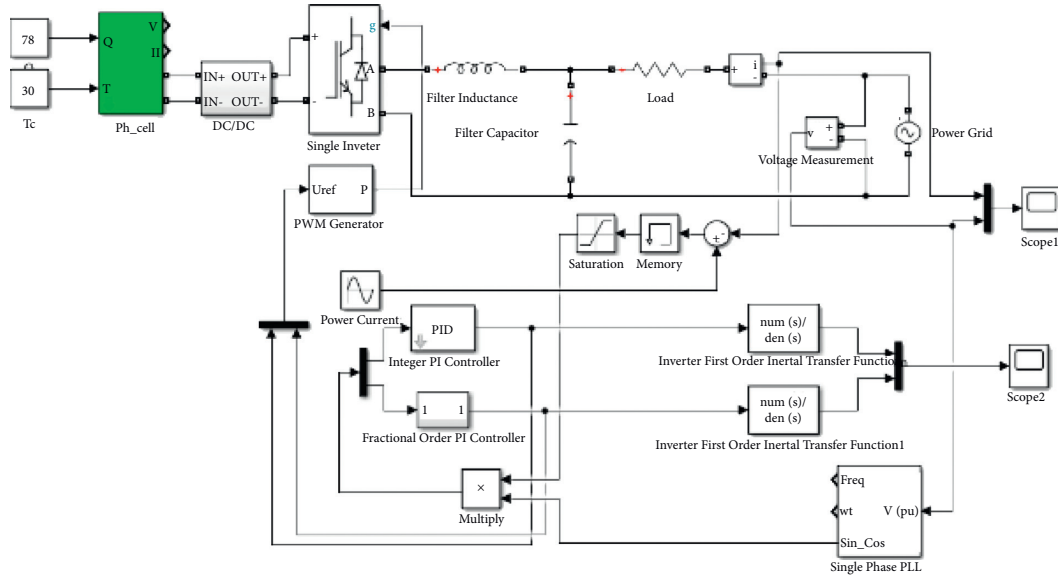


FIGURE 8: Single-phase photovoltaic grid current control strategy using MATLAB/Simulink simulation model.

TABLE 4: Simulation parameters.

Input voltage	400 V	Filter inductance	6 mH
Effective value of power network voltage	220 V	Equivalent resistance of filter inductance	0.5Ω
Power grid voltage frequency	50 Hz	Switching cycle	$100 \mu\text{s}$
Filter capacitor	$0.1 \mu\text{F}$	PWM frequency	5 kHz
Maximum voltage of PV	68 V	Maximum current of PV	59 A
Chopping frequency	5 kHz	Power of load	2 kW
The inductor of DC/DC	3 mH	Capacitor of DC/DC	$220 \mu\text{F}$

For the FO-PI controller, at the fundamental frequency ω_0 , the amplitude is $A(\omega_0)_2 = \sqrt{K_P^2 + (K_I/\omega_0^\lambda)^2}$; the integral order λ can take any real number greater than 0, and when λ gets the appropriate value on $(0, 1)$, $A(\omega_0)_2 \gg A(\omega_0)_1$; the

first term of equation (28) is closer to i_{ref} and the second term is closer to 0; thus, $\approx i_{\text{ref}}$. So, compared to the IO-PI controller, the FO-PI controller largely reduces the system steady-state error and enhances the system's antidisturbance capability.

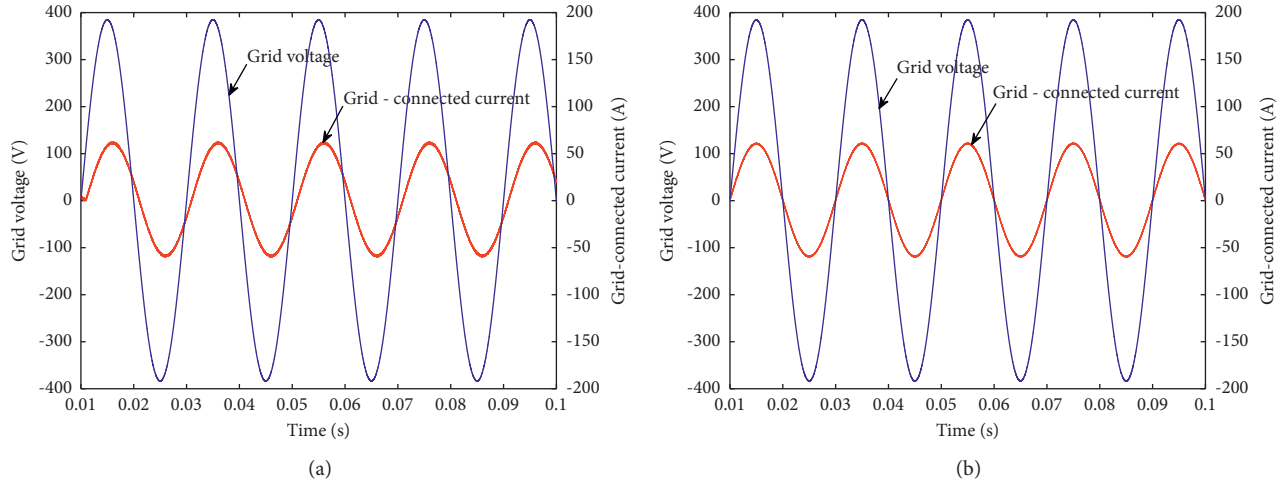


FIGURE 9: Grid current and grid voltage waveform. (a) IO-PI control grid current and grid voltage wave. (b) FO-PI control grid current and grid voltage wave.

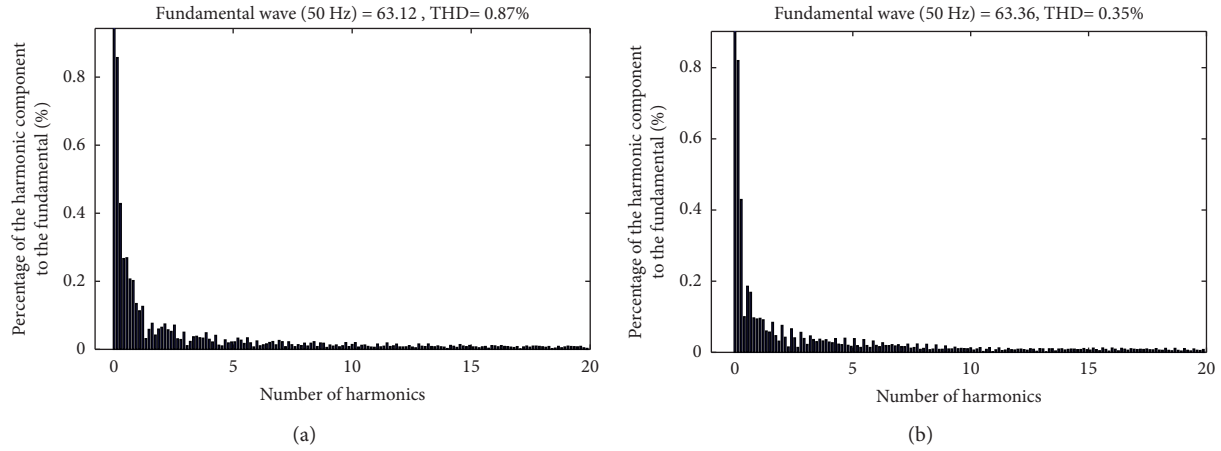


FIGURE 10: FFT analysis of grid-connected current of the (a) IO-PI controller and (b) FO-PI controller.

At the time of 0.05 s, the grid voltage disturbance, the grid voltage dips, and the change in the output current of the inverter is shown in Figure 7.

From Figure 7, we can see that the output current of the inverter under the control of IO-PI appears small fluctuations, while the output current of the inverter under FO-PI control is almost unchanged, which is not affected by the voltage disturbance of the grid. The result shows that the FO-PI controller has better anti-interference ability, and the system possesses strong robustness.

5. Simulation Result Analyses

The inverter link is the key to the whole PV grid-connected system, and it must be connected to the grid through an effective control strategy. According to GB/T 19935-2005 technical requirements for the grid connection of the PV system, the grid-connected current and grid voltage with the same frequency and phase and the total harmonic distortion (THD) of the grid-connected current should be less

than 5% of the inverter-rated output. The simulation model of the single-phase PV grid-connected current control is built using MATLAB/Simulink, as shown in Figure 8. The simulation parameters are shown in Table 4.

On the same control object, the waveform comparison of the grid voltage and the grid current by using IO-PI control and FO-PI control is shown in Figure 9. The corresponding grid current is analyzed by using the fast Fourier transform (FFT) algorithm, and the total harmonic distortion rate (THD) of the grid-connected current is illustrated in Figure 10.

The simulation results show that compared with the IO-PI controller, the grid-connected current and the grid voltage have smaller phase differences by using the FO-PI controller, which can effectively reduce the tracking error of the system. The THD of the grid-connected current of the IO-PI control and the FO-PI control was 0.87% and 0.35%, respectively, and the FO-PI controller is able to achieve grid-phase current and grid voltage with the same frequency and phase, and the current distortion rate is small.

6. Conclusion

In this paper, the PI^λ controller is applied to the single-phase PV grid-connected power generation system and tracking control of the output current of the grid-connected inverter. The PI^λ controller is designed by using the amplitude phase-frequency method, and the dynamic performance, steady-state performance, and robustness of the control system are simulated and compared with those of the integer-order PI controller. The results show that the PI^λ controller has faster response speed and better following performance than the fractional-order PI controller, which reduces the harmonic content of the grid-connected current, enhances the anti-interference of the system, and makes the system realize grid operation better.

Data Availability

The inverter system parameter data used to support the findings of this study are included within the article.

Conflicts of Interest

The authors declare that they have no conflicts of interest.

Acknowledgments

This work was supported by the Key Research and Development program (Key Projects) of Shaanxi Province (no. 2019KWZ-10), the Key Research and Development Program (General Projects) of Shaanxi Province (no. 2019KW-005), and Xi'an Science and Technology Plan Project (no. 2019218114GXRC017CG018-GXYD17.6).

References

- [1] S. Demirbas, "Self-tuning fuzzy-PI-based current control algorithm for doubly fed induction generator," *IET Renewable Power Generation*, vol. 11, no. 13, pp. 1714–1722, 2017.
- [2] C. Gao, Q. Chen, and L. Zhang, "Current multi-loop control strategy for grid-connected inverter with LCL filter," in *Proceedings of the 2018 33rd Youth Academic Annual Conference of Chinese Association of Automation (YAC)*, pp. 712–716, IEEE, Nanjing, China, May 2018.
- [3] Z. Xia, F. Xia, P. Cong, Z. Yang, H. Song, and X. Hong, "Grid connected control strategy of microgrid," *IOP Conference Series: Earth and Environmental Science*, vol. 170, no. 4, Article ID 042147, 2018.
- [4] S. Zheng, X. Tang, and B. Song, "Tuning strategy of fractional-order proportional integral controllers for permanent magnet synchronous motor servo system based on enhanced stochastic multi-parameters divergence-based optimisation algorithm," *IET Control Theory & Applications*, vol. 10, no. 11, pp. 1240–1249, 2016.
- [5] Y. Xie, X. Tang, B. Song, X. Zhou, and Y. Guo, "Model-free tuning strategy of fractional-order PI controller for speed regulation of permanent magnet synchronous motor," *Transactions of the Institute of Measurement and Control*, vol. 41, no. 1, pp. 23–35, 2019.
- [6] W. Zheng, Y. Luo, Y. Chen, and Y. Pi, "Fractional-order modeling of permanent magnet synchronous motor speed servo system," *Journal of Vibration and Control*, vol. 22, no. 9, pp. 2255–2280, 2016.
- [7] Y. Ding, L. Chen, and K. Hao, "Bio-Network inspired co-operative intelligent controllers," *Bio-Inspired Collaborative Intelligent Control and Optimization*, Springer, Singapore, pp. 233–277, 2018.
- [8] M. Obi and R. Bass, "Trends and challenges of grid-connected photovoltaic systems-a review," *Renewable and Sustainable Energy Reviews*, vol. 58, pp. 1082–1094, 2016.
- [9] A. Anzalchi and A. Sarwat, "Overview of technical specifications for grid-connected photovoltaic systems," *Energy Conversion and Management*, vol. 152, pp. 312–327, 2017.
- [10] Y. J. Lee, S. Y. Kim, and S. K. Han, "A study on the energy saving capacity of solar power generation system using economic evaluation," *The Transactions of the Korean Institute of Electrical Engineers P*, vol. 67, no. 1, pp. 21–26, 2018.
- [11] R. Hasan, S. Mekhilef, M. Seyedmahmoudian, and B. Horan, "Grid-connected isolated PV microinverters: a review," *Renewable and Sustainable Energy Reviews*, vol. 67, pp. 1065–1080, 2017.
- [12] G. Boukettaya, O. Naifar, and A. Ouali, "A vector control of a cascaded doubly fed induction generator for a wind energy conversion system," in *Proceedings of the 2014 IEEE 11th International Multi-Conference on Systems, Signals & Devices (SSD14)*, February 2014.
- [13] J. Wang, C. Shao, and Y.-Q. Chen, "Fractional order sliding mode control via disturbance observer for a class of fractional order systems with mismatched disturbance," *Mechatronics*, vol. 53, pp. 8–19, 2018.
- [14] O. Naifar, G. Boukettaya, and A. Ouali, "A comparative study between a high-gain interconnected observer and an adaptive observer applied to IM-based WECS," *The European Physical Journal Plus*, vol. 130, no. 5, pp. 1–13, 2015.
- [15] A. Tepljakov, B. B. Alagoz, C. Yeroğlu, E. Gonzalez, S. H. Hosseinia, and E. Petlenkov, "FOPID controllers and their industrial applications: a survey of recent results 1 This study is based upon works from cost action CA15225, a network supported by cost (European cooperation in science and Technology)," *IFAC-PapersOnLine*, vol. 51, no. 4, pp. 25–30, 2018.
- [16] C. Knoll and R. Heedt, "Automatic control knowledge repository—a computational approach for simpler and more robust reproducibility of results in control theory," in *Proceedings of the 2020 24th International Conference on System Theory, Control and Computing (ICSTCC)*, pp. 130–136, IEEE, Sinaia, Romania, October 2020.
- [17] O. Naifar, G. Boukettaya, and A. Ouali, "Robust software sensor with online estimation of stator resistance applied to WECS using IM," *International Journal of Advanced Manufacturing Technology*, vol. 84, no. 5-8, pp. 885–894, 2016.
- [18] M. Lu, Y. Yang, and B. Johnson, "An interaction-admittance model for multi-inverter grid-connected systems," *IEEE Transactions on Power Electronics*, vol. 34, no. 8, pp. 7542–7557, 2018.